

# Cohesive analysis of a 3D benchmark for delamination growth under quasi-static and fatigue loading conditions

Antonio Raimondo<sup>1</sup>  | Carlos G. Dávila<sup>2</sup> | Chiara Bisagni<sup>1</sup> 

<sup>1</sup>Faculty of Aerospace Engineering, Delft University of Technology, Delft, The Netherlands

<sup>2</sup>Durability, Damage Tolerance and Reliability Branch, NASA Langley Research Center, Hampton, Virginia, USA

## Correspondence

Antonio Raimondo, Delft University of Technology, Faculty of Aerospace Engineering, Delft, The Netherlands.  
Email: [a.raimondo@tudelft.nl](mailto:a.raimondo@tudelft.nl)

## Funding information

European Union's Horizon 2020, Grant/Award Number: 707404

## Abstract

This paper evaluates the capabilities of the recently developed CF20 cohesive fatigue model, which can predict crack initiation as well as the rates of crack propagation by relying on intrinsic relationships between a stress-life diagram and its corresponding Paris law. The model is validated here using a partially reinforced double cantilever beam (R-DCB) benchmark proposed in literature. The two parameters needed for the CF20 cohesive fatigue model were obtained by performing preliminary analyses of a conventional DCB. The analysis results indicate that the CF20 cohesive fatigue model can accurately reproduce the complex evolution of the delamination observed in the R-DCB.

## KEYWORDS

cohesive zone model, delamination, fatigue, Paris law, S-N diagram

## 1 | INTRODUCTION

Fatigue is a major concern in the design of high-performance composite structures, where high operating strains, post-buckling deformations, manufacturing imperfections, or stress concentrations can induce delaminations and a subsequent loss of structural integrity.<sup>1</sup> To mitigate such failures, the effect of fatigue damage mechanisms must be evaluated from the earliest stages of design using validated and computationally efficient numerical tools. Validated numerical methodologies would allow the application of a damage tolerance approach for the certification of composite structures in which the damage growth is predicted, and inspection intervals are defined.

For a numerical methodology to be useful for predicting fatigue, it must meet two basic requirements. First, its capabilities must be validated using test cases that are well controlled and realistic. Second, the

methodology must rely on model parameters that can be obtained from material characterization tests. However, due to a lack of accurate benchmark cases, the validation of fatigue damage models is often reduced to calibrating the models to fit a desired experimental result. In addition, most well-controlled tests have overly simple configurations, such as those of a double cantilever beam (DCB) or mixed mode bending (MMB) test. Fitting a model to the experimental results of a simple specimen such as a DCB or an MMB test does not ensure the ability of the numerical methodology to predict the responses of more complex structural problems.

Due to the cost and time required to generate them, relatively few results of experimental fatigue tests exhibiting any structural complexity can be found in the literature. Several investigations concern the propagation of fatigue cracks in notched and open hole specimens.<sup>2–4</sup> Sachse et al. investigated the rates of crack propagation in bonded joints.<sup>5</sup> Dávila et al. performed testing and

This is an open access article under the terms of the [Creative Commons Attribution-NonCommercial-NoDerivs](https://creativecommons.org/licenses/by-nc-nd/4.0/) License, which permits use and distribution in any medium, provided the original work is properly cited, the use is non-commercial and no modifications or adaptations are made.

© 2022 The Authors. *Fatigue & Fracture of Engineering Materials & Structures* published by John Wiley & Sons Ltd.

analysis of postbuckled stiffened panels subjected to cyclic loading.<sup>6,7</sup> Murri et al. and Zhang et al. developed analyses for the durability of tapered composite beams subjected to combined loads.<sup>8,9</sup> Liang et al. demonstrated the ability of an extended finite element model to predict the ply migration of fatigue-driven delaminations.<sup>10</sup> However, test cases where the delamination does not evolve in a self-similar manner are often too complex both in terms of configuration, response, and failure modes to be used as a benchmark for the validation of numerical damage models focused on the propagation of delamination.

With the aim of providing a test case for the validation of delamination growth in a three-dimensional problem under static and fatigue loads, Carreras et al.<sup>11</sup> proposed a specimen called the reinforced double cantilever beam (R-DCB). The specimen is similar to a DCB but with partial-width reinforcement plates on both the top and bottom surfaces of the specimen. The reinforcement plates cover a portion of the width and length of the specimen. Although the configuration of the specimen is simple, the response of the R-DCB is relatively complex and is characterized by severe variations in the propagation rates and a delamination front that changes during the test. In addition, the benchmark provides a detailed set of material properties, including the Paris law fatigue data corresponding to a standard DCB specimen.

Predicting the response of the R-DCB specimen with cohesive fatigue models poses several challenges. Most cohesive fatigue models rely on Paris law data and require non-local information for the calculation of the length of the process zone and the energy release rate.<sup>12</sup> Several approaches have been developed to address the nonlocality of these models. Harper<sup>13</sup> and Teimouri<sup>14</sup> estimated the length of the process zone by performing preliminary quasi-static analyses. In the *thick level set method*,<sup>15</sup> the length of the process zone is set by a signed distance function that keeps track of the continuously moving damage front. Bak<sup>16</sup> and Carreras<sup>17</sup> proposed fatigue methodologies that perform a J-integral evaluation of the process zone and rely on the assumption that the distributions of traction and opening displacement in the damage process zone and the length of the process zone do not change in the shift from quasi-static to fatigue loading and back. As these models indicate, addressing the nonlocality of the fracture process zone length requires significant numerical complexity.

A second difficulty associated with fatigue cohesive models based on the Paris law is that the Paris law does not describe the initiation of fatigue cracks. Therefore, these models are often complemented with an additional criterion based on S-N test data.<sup>18</sup> These additional data required for these models are a significant burden to their

use in practical applications. Other limitations of the Paris law are that it is expensive to characterize for all load ratios and mode-mixities, and it does not uniquely describe the R-curve effects nor the propagation of short cracks.

Some local cohesive fatigue formulations have been proposed that are not based on the Paris law,<sup>19</sup> but these models require problem-specific calibration of the input properties. For example, Pan<sup>20</sup> performed analyses of the R-DCB using model parameters obtained by fitting the analysis results to the experimental results. In contrast, the present investigation relies on the mixed-mode CF20 cohesive fatigue formulation<sup>21</sup> and input properties that can be obtained from a single fatigue characterization test. This model is based on the stress-life response (S-N diagram) rather than on the rate of crack propagation described by the Paris law. CF20 is a unified fatigue model that can predict crack initiation as well as the rates of crack propagation by relying on intrinsic relationships between an S-N diagram and its corresponding Paris law.<sup>22,23</sup> The main benefit of the CF20 model is that it requires only three parameters, one of which is optional and was not investigated within the scope of the present effort. The model uses engineering approximations such as the Goodman diagram to synthesize S-N curves that account for any mode-mixity or stress ratio.<sup>22</sup> In addition, the model is easy to implement because it is purely local; that is, the damage at an integration point only depends on the accumulated history of the cyclic stresses. Liang<sup>10</sup> adopted the CF20 model to simulate a clamped tapered beam (CTB) subelement focusing on crack initiation and delamination migration. The innovative aspect of the present study is that it demonstrates that the evolution of a relatively complex delamination front can be predicted based on few independently characterized properties and without adjustments based on expected outcome. In previous investigations of the CF20 model, simple specimens such as the DCB and MMB were used to obtain the model parameters and then to verify the results. When modeling more complex structural configurations, where a precise experimental characterization of the damage propagation is impractical, and where the models rely on a number of properties and parameters that can be adjusted, it is not possible to perform a direct unadjusted validation of the models. In this paper, the CF20 is applied to analyze the R-DCB benchmark that was specifically developed to validate the capabilities of the model in simulating fatigue crack propagation models in a three-dimensional configuration where the crack front evolves in a complex manner under a large range of propagation rates.

The remainder of this paper is organized as follows. Section 2 briefly summarizes the CF20 fatigue cohesive

constitutive model and its implementation as a UMAT user subroutine within Abaqus.<sup>24</sup> In Section 3, the procedure to determine the parameters of the fatigue damage models is described. Then, the R-DCB benchmark is described and the numerical results are presented and compared with the experimental data. Finally, an analysis is performed to evaluate the sensitivity of the present methodology to the calibration of the model parameters.

## 2 | COHESIVE FATIGUE MODEL BASED ON THE S-N DIAGRAM

The S-N diagram describes the number of cycles to failure ( $N$ ) for a given maximum stress ( $S$ ) and stress ratio ( $R = \sigma_{min}/\sigma_{max}$ ). For quasi-brittle materials, an S-N diagram can be approximated by a straight line in a log-log plot, so an entire diagram can be described by the quasi-static strength,  $\sigma_c$ , plus the endurance limit,  $\sigma_e$ , defined as the maximum stress that a material can sustain for at least  $10^7$  load cycles without failure. The relative endurance limit for a given  $R$  ratio,  $E = \sigma_{eR}/\sigma_c$ , can be estimated from the relative endurance at  $R = -1$  (full load reversal),  $\varepsilon = \sigma_e/\sigma_c$ , using the Goodman diagram.<sup>21</sup> The resulting expression for the relative endurance limit as a function of the stress ratio is

$$E = \frac{\sigma_{eR}}{\sigma_c} = \frac{2\varepsilon}{\varepsilon + 1 + R(\varepsilon - 1)} \quad (1)$$

The CF20 cohesive fatigue model<sup>21</sup> assumes that the rate of damage accumulation at a point  $P$  is a function of the relative displacement jump  $\lambda/\lambda^*$  shown in Figure 1. The damage rate set by the CF20 model follows a power law of the form:

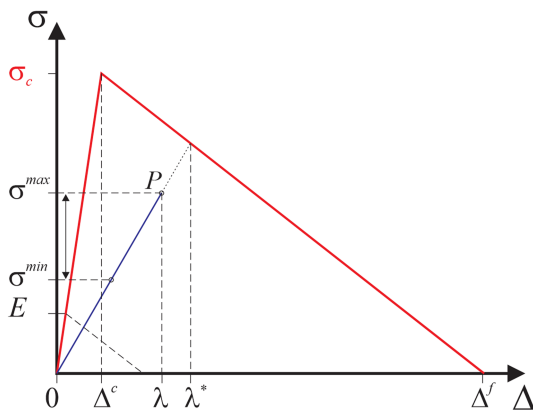


FIGURE 1 Bilinear cohesive law with fatigue damage [Colour figure can be viewed at [wileyonlinelibrary.com](http://wileyonlinelibrary.com)]

$$\frac{dD}{dN} = \frac{1}{\gamma} \frac{(1-D)^{\beta-p}}{E^{\beta}(p+1)} \left( \frac{\lambda}{\lambda^*} \right)^{\beta} \quad (2)$$

where  $D$  is the damage norm defined as

$$D = \frac{\lambda^* - \Delta^c}{\Delta^f - \Delta^c} \quad (3)$$

and where  $\gamma = 10^7$  is the number of cycles at the endurance,  $\beta$  represents the slope of the S-N curve, and  $p$  is a model parameter. Only two of the parameters are independent, as described at the end of this section. The relative displacement jump at a point  $P$  is

$$\frac{\lambda}{\lambda^*} = \frac{\sigma^{\max}}{(1-D)\sigma_c} \quad (4)$$

The damage within the cohesive element accumulates with load cycles unless the relative displacement falls below the endurance,  $E$ . To ensure that Equation 2 reproduces an S-N curve that includes the desired endurance point, the exponent  $\beta$  in Equation 2 is defined as

$$\beta = \frac{-7\eta}{\log E} \quad (5)$$

where the optional parameter  $\eta$  is a “brittleness parameter.” Its purpose is to take into account within the model of the low-cycle “hump” in the S-N diagram of a material subjected to high cyclic stresses. For  $\eta = 1$ , the log-log plot of an S-N diagram is a straight line, while decreasing the value of  $\eta$  results in a low-cycle plateau, as illustrated in Figure 2A. In the analyses performed herein, a brittleness parameter of  $\eta = 0.95$  is assumed based on Dávila et al.,<sup>21</sup> which means that the fatigue accumulation function described by Equation 2 depends on only two parameters:  $\varepsilon$  and  $p$ . As Figure 2A,B illustrates, the parameter  $\varepsilon$  affects the slopes of the S-N and Paris curves, and increasing  $p$  moves the Paris curve up. The effect of the parameter  $p$  on the S-N diagram is negligible.

The proposed fatigue damage formulation is capable of accounting for an R-curve increase of the energy release rate with crack propagation using a superposition of two bilinear cohesive elements.<sup>21,22</sup> The CF20 cohesive damage constitutive model was implemented in Abaqus by means of a User Material Subroutine (UMAT).<sup>24</sup> The finite element analyses were performed using a simplified cyclic loading (SCL) procedure, in which the maximum load is kept constant, and the cyclic nature of the load is taken into account by the cohesive constitutive model by

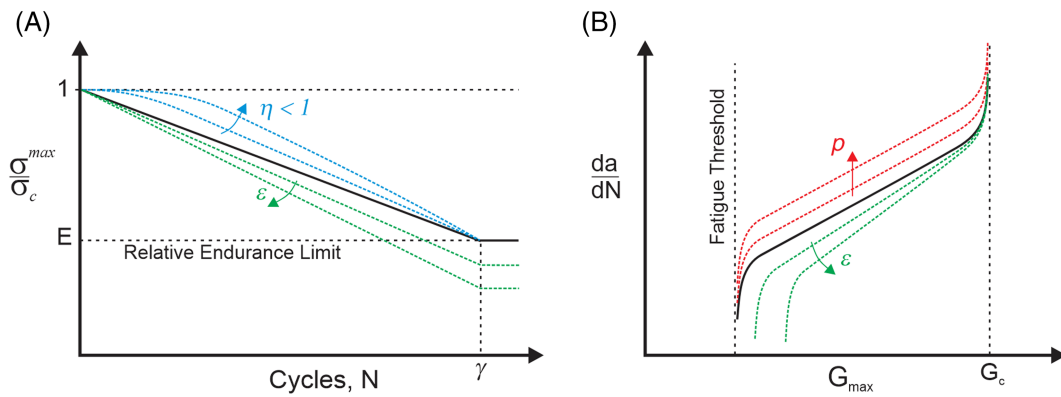


FIGURE 2 Effect of the model parameters  $\eta$ ,  $\epsilon$ , and  $p$  on: (A) S-N diagram and (B) crack propagation curve [Colour figure can be viewed at [wileyonlinelibrary.com](http://wileyonlinelibrary.com)]

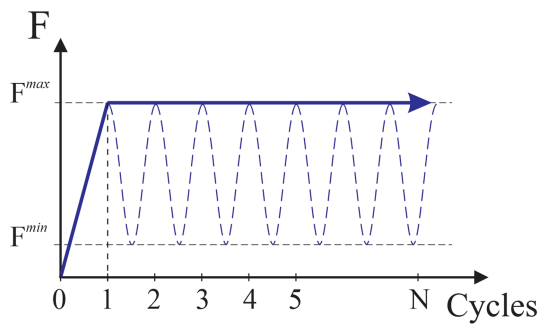


FIGURE 3 Simplified cyclic loading (SCL) procedure [Colour figure can be viewed at [wileyonlinelibrary.com](http://wileyonlinelibrary.com)]

specifying the stress ratio,  $R$ , in Equation 1. The analysis is divided in two steps: In the first step, the load is increased up to its maximum value. During this step, quasi-static damage is enabled, and fatigue damage is not. In the second step, the maximum load is kept constant, and the fatigue damage accumulation model is activated. During this second step, the pseudo-time of the analysis represents the cycle count. The SCL procedure is illustrated in Figure 3.

### 3 | DETERMINATION OF THE FATIGUE MODEL PARAMETERS

As discussed in the previous section, the CF20 cohesive fatigue model requires two parameters:  $\epsilon$  and  $p$ . The first parameter affects the slope of the S-N and Paris law curves, and the second one affects the pre-factor  $C$  of the calculated Paris law but does not affect the S-N curve. Therefore, both parameters can be obtained from a single experimental Paris law. Since the model accounts for the stress ratio,  $R$ , the characterization of the parameters can be performed using experimental results for any value of  $R$ .

The R-DCB benchmark includes Paris law data acquired from conventional DCB specimens. This data was used to determine the parameters of the CF20 fatigue model. The experimental procedure described in previous studies<sup>25,26</sup> was reproduced herein using the model shown in Figure 4. The DCB specimen consists of a rectangular plate 250 mm long and 25 mm wide, manufactured using 16 unidirectional plies with a total thickness of 3 mm and an initial delamination length of 60 mm.

Two layers of continuum SC8R shell elements were used to represent each arm of the specimen. A parametric FE model was developed to perform mesh sensitivity analyses and determine the size of the elements. The elements in the refined area intended for delamination propagation have a length of 0.1 mm, while those outside of this area have a length of approximately 2 mm. The two arms are connected to each other by a layer of zero-thickness cohesive elements (COH3D8).

The material properties provided with the benchmark are reported in Table 1. The normal interfacial strength,  $\sigma_c$ , is the only required property not provided by the benchmark, and a value of 70 MPa was selected. This value is sufficiently high to ensure that the length of the process zone is reasonably small. Problems without pre-existing cracks, where the role of the strength is essential to predict initiation, may require a more careful evaluation of the interfacial strength.

As in the experiments, the analyses were conducted under displacement control with a maximum applied displacement of 6.5 mm and  $R = 0.1$ .

The length of the delamination and the crack growth rate were evaluated using the equations derived from the corrected beam theory.<sup>27</sup> These equations provide the means to calculate the crack length and the energy release rate from the compliance of the specimen ( $C = \delta_{max}/F$ ), which only depends on the calculated

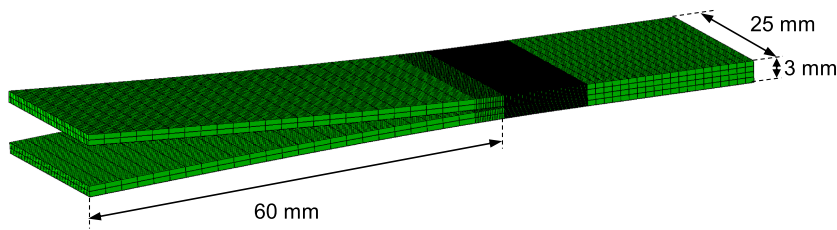


FIGURE 4 DCB model used for the calibration of the CF20 model [Colour figure can be viewed at [wileyonlinelibrary.com](http://wileyonlinelibrary.com)]

TABLE 1 Material properties for the numerical simulation<sup>11</sup>

Property	Unit	Value
$E_1$	MPa	154,000
$E_2$	MPa	8500
$G_{12}$	MPa	4200
$\nu_{12}$		0.35
$G_{1C}$	kJ/m <sup>2</sup>	0.305
$\sigma_c$	MPa	70

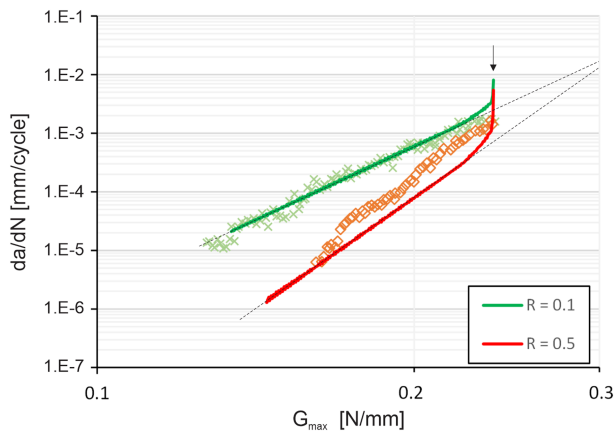


FIGURE 5 Numerical (lines) and experimental (symbols<sup>26</sup>) crack growth rates for DCB specimen for two values of the load ratio  $R$  (Model parameters:  $\varepsilon = 0.23$ ,  $p = \beta + 1$ ) [Colour figure can be viewed at [wileyonlinelibrary.com](http://wileyonlinelibrary.com)]

reaction force,  $F$ , and the constant applied displacement,  $\delta_{max}$ .

The expressions for the crack length and the energy release rate are

$$a = \left( \frac{3}{2} C EI \right)^{1/3} - \chi h \quad G_I = \frac{(a + \chi h)^2}{bEI} F^2 \quad (6)$$

where  $b$  is the width of the specimen and  $h$  is the thickness of each arm and

$$\chi = \sqrt{\frac{E_1}{11G_{13}} \left[ 3 - 2 \left( \frac{\Gamma}{1 + \Gamma} \right)^2 \right]} \quad (7)$$

$$\Gamma = 1.18 \frac{\sqrt{E_1 E_2}}{G_{13}} \quad EI = E_1 \frac{bh^3}{12}$$

The parameters  $\varepsilon$  and  $p$  were determined as follows. A parametric study was conducted, starting with the values suggested in Dávila et al.<sup>21</sup>:  $\varepsilon = 0.2$  and  $p = \beta$ . Then, the value  $\varepsilon$  was perturbed, and additional analyses were performed to fit the slope of the calculated Paris line to the DCB experimental results<sup>26</sup> for  $R = 0.1$  (green crosses in Figure 5). Finally, the value of  $p$  was perturbed until the calculated Paris line aligned with the experimental results. The final results in terms of crack growth rate as a function of the maximum value of the energy release rate ( $G_{max}$ ) shown in green in Figure 5 correspond to  $\varepsilon = 0.23$ ,  $p = \beta + 1$ . It can be observed that the initial rate of propagations is highest. Once the crack propagates approximately 1 mm and the process zone fully forms, the rate of propagation follows a Paris line.

In principle, the determination of the model parameters can be performed by using test data for any stress ratio, and these parameters can then be used in analyses with other stress ratios. The two Paris lines reported in Figure 5 are obtained using the same values of  $\varepsilon$  and  $p$ , and those values are calculated by fitting the numerical results with the experimental data at  $R = 0.1$ , since the benchmark is only tested at this value of the stress ratio. However, these results indicate that the analysis results for  $R = 0.5$  underpredict the experimental results (red symbols) by approximately 50%. Despite this inaccuracy, it can be observed that the experimental Paris lines intersect at approximately  $G_{max} = 0.25$  N/mm, while the analysis results intersect slightly above  $G_{max} = 0.3$  N/mm. As expected from theoretical observations,<sup>23</sup> the Paris lines at different stress ratio should intersect around a value of  $G$  close to the fracture toughness, which is the case with the numerical results and not with the experimental data. This observation points to the difficulties and uncertainty associated with performing fatigue testing and the



potential errors in the characterization of fatigue properties. A more detailed discussion on the sensitivity of the calibration of the model parameters will be given in Section 7.

#### 4 | R-DCB BENCHMARK

The specimen used in the R-DCB benchmark<sup>11</sup> is a conventional DCB with unidirectional reinforcement plates bonded to each arm. The reinforcements do not extend over the entire length or width of the specimen, which forces the delamination front to curve during propagation. The configuration of the specimen is shown in Figure 6. The material properties reported in Table 1 have been considered in the numerical analyses, since the R-DCB benchmark and the DCB specimens have been manufactured with the same material.

The loading sequence for the R-DCB benchmark consists of four steps. First, the top arm is displaced quasi-statically up to an opening displacement of 5 mm. In a second step, a cyclic load is applied with a maximum displacement of 5 mm and a load ratio of  $R = 0.1$  for 410,000 cycles. At the end of Step 2, the applied displacement is increased to 10 mm, after which a second fatigue step starts with an applied maximum displacement of 10 mm for 10,000 cycles. The sequence of steps is illustrated in Figure 7.

Although simple in terms of geometry, the R-DCB benchmark test exhibits a relatively complex evolution of the delamination front. In addition, the loading conditions induce a broad range of propagation rates, ranging from quasi-static tearing to less than 1 mm of growth per 100,000 cycles.

The R-DCB benchmark provides the experimental results needed to validate fatigue models. The results provided include the location and shape of the delamination front obtained with an automated X-ray image processing procedure during propagation. Several specimens were tested to demonstrate repeatability.<sup>11</sup>

#### 5 | ANALYSIS OF R-DCB BENCHMARK TEST

The R-DCB specimen is symmetric in terms of geometry, material, and boundary conditions about  $y-z$  and  $x-z$  planes. Both symmetry planes were used to reduce the size of the model such that only one quarter of the specimen and half of one arm was modeled. The discretization adopted in Section 3 in the analysis of DCB specimen was followed as closely as possible: Two layers of SC8R continuum shell elements were used through the thickness of the unreinforced sections of the arms, and two more were used for the reinforcements. The element length in the refined region of propagation is 0.1 mm. The  $x-y$  symmetry was enforced by tying the  $x$ - and  $y$ -direction displacements of the nodes at the bottom surface of the cohesive layer to the corresponding displacements of the nodes on the top surface of the cohesive layer. The  $z$ -direction displacement of the bottom plane was constrained. Since the opening displacements of the cohesive elements represent half of the actual opening, a critical energy release rate of  $G_c/2$  was used. The boundary conditions for a typical cohesive element are illustrated in Figure 8.

All the nodes along the loaded edge of the R-DCB were rigidly connected to a single node where the

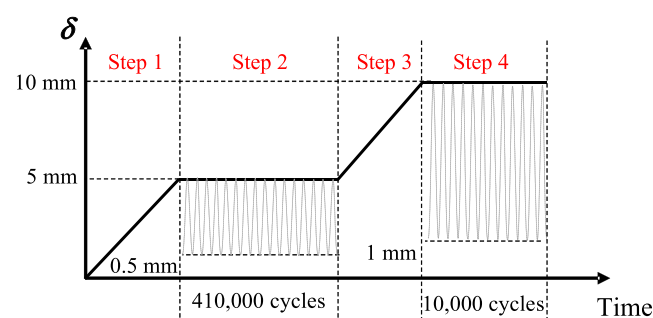


FIGURE 7 Sequence of steps for R-DCB<sup>11</sup> [Colour figure can be viewed at [wileyonlinelibrary.com](http://wileyonlinelibrary.com)]

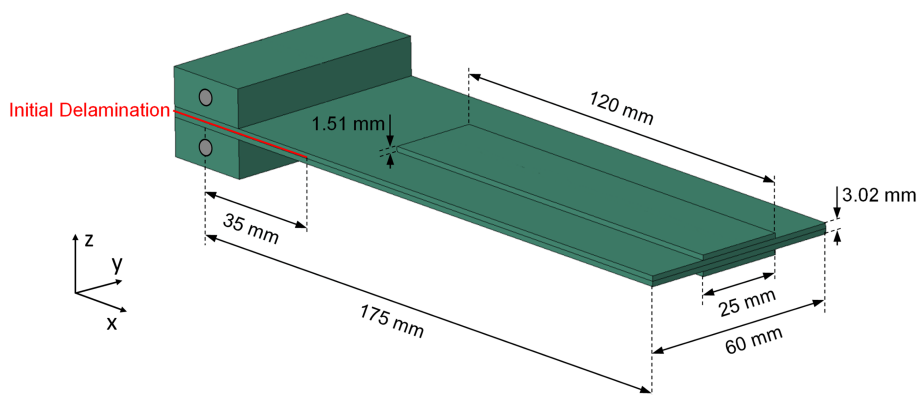


FIGURE 6 R-DCB geometrical dimensions<sup>11</sup> [Colour figure can be viewed at [wileyonlinelibrary.com](http://wileyonlinelibrary.com)]

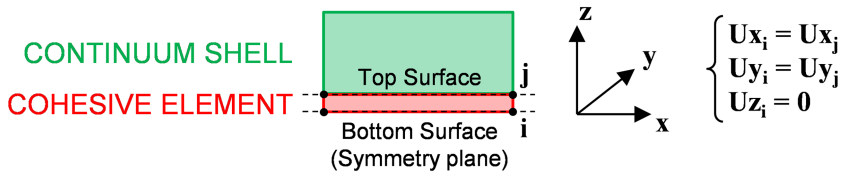


FIGURE 8 Symmetry boundary condition on a generic cohesive element [Colour figure can be viewed at [wileyonlinelibrary.com](http://wileyonlinelibrary.com)]

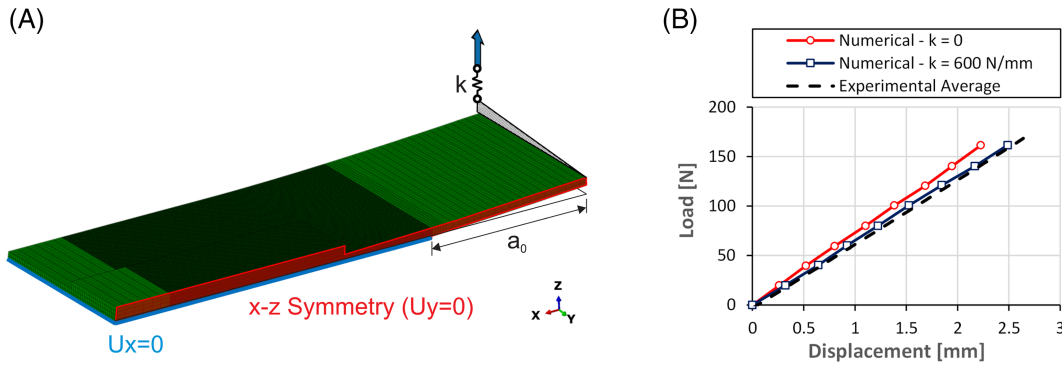


FIGURE 9 (A) Finite element model of R-DCB test; (B) influence of the spring on the initial stiffness [Colour figure can be viewed at [wileyonlinelibrary.com](http://wileyonlinelibrary.com)]

displacement was applied through a spring with a stiffness of  $k = 600$  N/mm (Figure 9A). The spring is used to compensate for a discrepancy in the initial stiffness between the numerical and the experimental results, which is presumably due to compliance of the loading blocks and testing machine (Figure 9B). The  $x$ - $z$  symmetry was applied by constraining the  $y$ -direction displacements of the nodes on the plane of symmetry.

## 6 | RESULTS AND COMPARISONS

The numerical analysis was performed under displacement-controlled conditions in four loading steps (Figure 7) using the model parameters  $\epsilon = 0.23$  and  $p = \beta + 1$  obtained in Section 4. In the first quasi-static step, the displacement of the top arm is increased up to the maximum opening displacement of 5 mm. Only the static damage calculation is considered during this step, but the fatigue damage is not. In the second step, the applied displacement is kept constant and the fatigue damage calculation is enabled with a load ratio of  $R = 0.1$ . The maximum opening displacement is applied for 410,000 cycles. In the third step, fatigue damage is again disabled, and the displacement is quasi-statically increased up to 10 mm. For the fourth and final step, fatigue damage is reactivated with a load ratio of  $R = 0.1$  while the applied maximum displacement is maintained constant for 10,000 cycles. In all four steps, the time increments used for the analysis are automatically selected by Abaqus according to its default convergence

parameters. However, to ensure accuracy of the calculation, the time increment is cut in half when the maximum damage increment in the model exceeds 0.15. Therefore, approximately six to eight analysis increments are required per row of elements, which results in a total of about 2500 increments, or about 13 h in the high performance computing (HPC) cluster at TU Delft. The calculated and experimental reaction forces for the R-DCB benchmark are shown in Figure 10. The three gray lines represent experimental data provided by the benchmark, and the blue line corresponds to the present analysis.

As can be observed in the Figure 10, the reaction force reaches a maximum at an applied displacement of around 3 mm. Then, the delamination starts to propagate and the load decreases. When the displacement reaches the value of 5 mm, the fatigue analysis starts. The maximum displacement is held constant while the stiffness decreases due to the propagation of the delamination. The quasi-static/fatigue sequence is repeated with Steps 3 and 4. The largest errors in the analyses correspond to the latter parts of the two quasi-static steps. In particular, the analysis overestimates by 9% the load at the end of Step 3.

The shapes of the delamination fronts at three stages of Step 2 are shown in Figure 11. The upper half of the figure corresponds to three experimental results, and the lower part corresponds to the analysis results, where the red area represents the damaged (open) region of cohesive elements, and the blue area represents the intact region of the interface. The damage process zone, where the value of the cohesive damage variable is between

FIGURE 10 Load–displacement curves of the R-DCB ( $\epsilon = 0.23$ ,  $p = \beta + 1$ ) [Colour figure can be viewed at [wileyonlinelibrary.com](http://wileyonlinelibrary.com)]

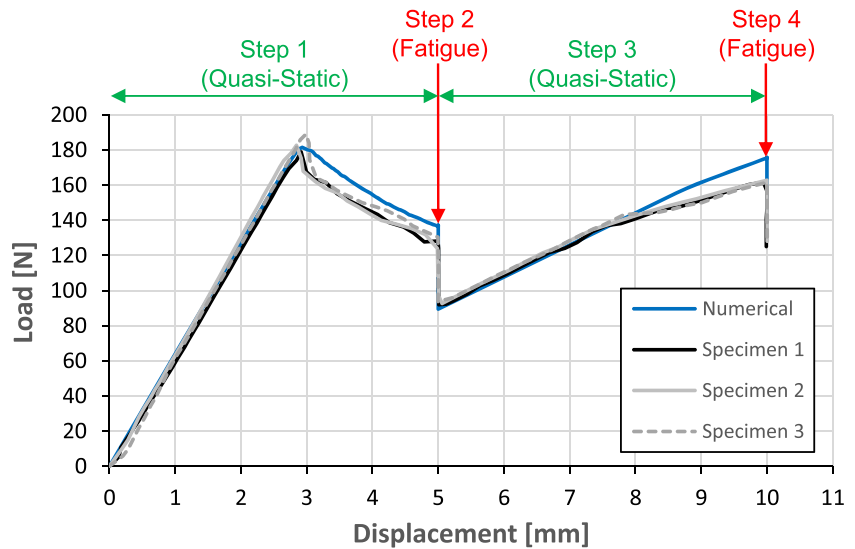


FIGURE 11 Comparison between numerical and experimental delamination front at three different load cycles counts of Step 2 ( $\epsilon = 0.23$ ,  $p = \beta + 1$ ) [Colour figure can be viewed at [wileyonlinelibrary.com](http://wileyonlinelibrary.com)]

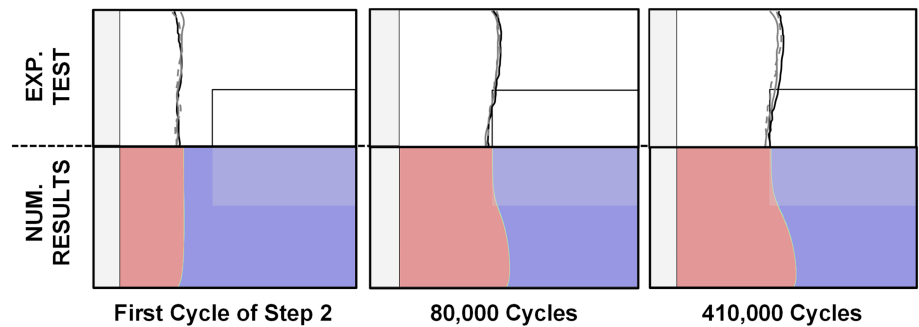
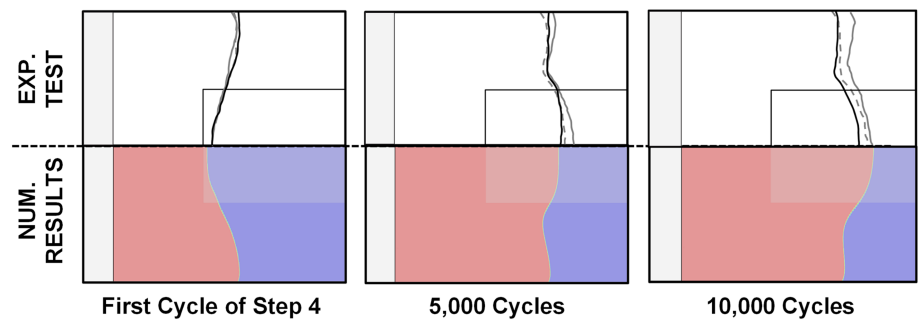


FIGURE 12 Comparison between numerical and experimental delamination front at different load cycles counts of Step 4 ( $\epsilon = 0.23$ ,  $p = \beta + 1$ ) [Colour figure can be viewed at [wileyonlinelibrary.com](http://wileyonlinelibrary.com)]



0 and 1, is narrow and appears as a faint green line separating the damaged and undamaged regions.

The initial delamination front has a mildly curved shape, where the anticlastic curvature causes a slight increase in the propagation at the center of the specimen compared to the edges. As the delamination front approaches the edge of the reinforcement, the balance of the crack opening displacements across the width of the specimen is altered by the local increase in stiffness, and the curvature of the delamination front reverses. As expected in a displacement-controlled test, the growth rate is initially high, with a rate of about 3 mm per 1000 cycles, and it rapidly decreases to less than 0.01 mm

per 1000 cycles at the end of the step. The agreement between numerical and experimental data in terms of delamination front position and shape is generally good, although the numerical analysis somewhat overestimates the propagation at the free edge of the specimen.

The quasi-static opening displacement of 10 mm applied in Step 3 induces a delamination front that enters the zone under the reinforcement plates. This quasi-static step is followed by the final fatigue step. The length of the fracture process zone is approximately 0.4 mm during the static step and around 0.3 mm during the fatigue step. As the results in Figure 12 indicate, the fatigue propagation rate at the center of the specimen is seen to increase



relative to the edges due to the internal load redistribution induced by the reinforcements. As a result, the curvatures of the delamination front reverse once again.

The crack growth rate measured at the center of the specimen starts at approximately 3 mm per 1000 cycles and reduces to about 1 mm per 1000 cycles after 10,000 additional cycles. The numerical model accurately predicts the crack growth rates as well as the changes in shape of the delamination front.

The differences in the crack growth rate between the two fatigue steps can also be appreciated in Figure 13, where the calculated compliance of the R-DCB is reported as a function the number of cycles. The large rate of increase in compliance observed in Step 4 is an indication of a faster propagation of the delamination.

### 7 | SENSITIVITY OF DELAMINATION LENGTH TO $da/dN$

In this section, the results of a numerical evaluation of the sensitivity of the model to the experimental characterization of the crack growth rate and to the calibration of the model parameters are presented.

A parametric analysis was conducted assuming a constant value of the parameter  $\beta$  in the CF20 model to evaluate the effect of the parameter  $p$  on the crack growth rate and the final position of the delamination front of the R-DCB specimen. Three fatigue analyses using different values of  $p$  were performed of the conventional DCB specimen discussed in Section 4. The resulting crack growth rates are compared in Figure 14. The dashed line corresponds to the experimentally determined Paris law parameters provided by the benchmark.<sup>11</sup>

As already remarked in Section 2, an increase in the parameter  $p$  corresponds to an upward shift of the crack

growth rate curves. Although all the numerical crack growth rates shown in Figure 14 are within the experimental scatter band, a best fit of the Paris line provided by the benchmark (dashed line) is obtained using  $p = \beta + 1.5$ . However, apparently small differences in the crack growth rate of the DCB can result in rather large variations in the predicted length of propagation and the shape of the delamination front. Indeed, errors in crack growth rates reported in a log-log plot can be misleading: a constant offset between two curves corresponds to an exponential increase in the error as the maximum energy release increases. Furthermore, even small errors in the crack growth rate curves may result in large errors in the predicted crack length over thousands of cycles.

In Figure 15, the numerical delamination front shape of the R-DCB obtained using a value of  $p = \beta + 1.5$  is

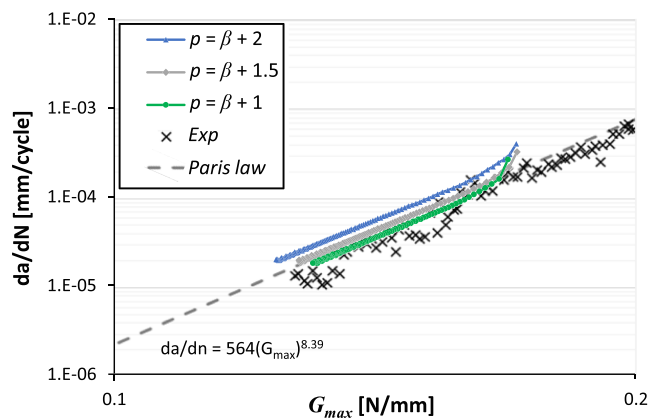


FIGURE 14 Comparison between numerical and experimental crack growth rate for DCB specimen at different values of the parameter  $p$  ( $\epsilon = 0.23$ )<sup>26</sup> [Colour figure can be viewed at [wileyonlinelibrary.com](http://wileyonlinelibrary.com)]

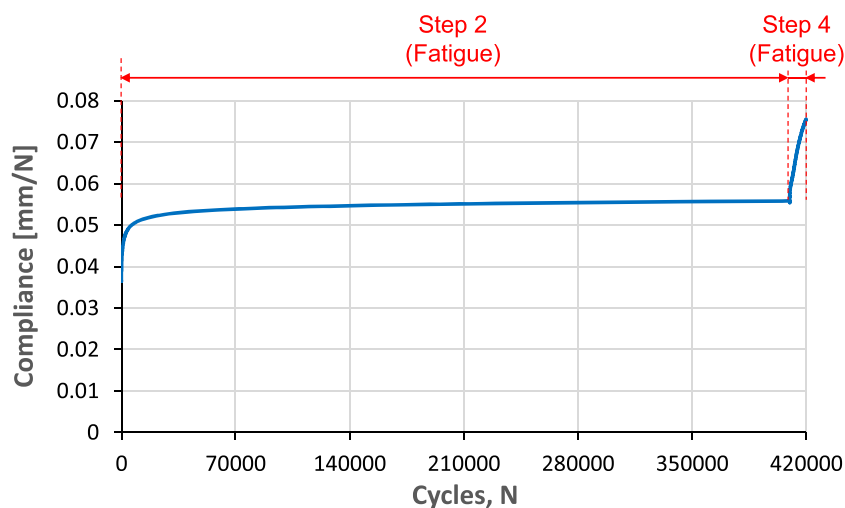
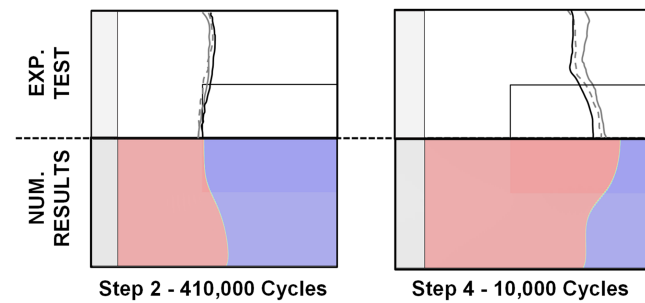


FIGURE 13 R-DCB compliance versus number of cycles [Colour figure can be viewed at [wileyonlinelibrary.com](http://wileyonlinelibrary.com)]



**FIGURE 15** Comparison between numerical and experimental delamination front at the end of Step 2 and Step 4 ( $\varepsilon = 0.23$ ,  $p = \beta + 1.5$ ) [Colour figure can be viewed at [wileyonlinelibrary.com](https://onlinelibrary.wiley.com/doi/10.1111/ffe.13712)]

compared with the experimentally measured crack fronts at the end of Steps 2 and 4. It can be observed that at the end of Step 2 the numerical delamination front shape is similar to the experimental delamination front and to the numerical results shown in Figure 10. For this step, the maximum displacement is relatively low, and the value of the energy release rate is small. At the end of Step 2, the difference in the crack growth rates between  $p = \beta + 1$  and  $p = \beta + 1.5$  is negligible. On the other hand,  $G_{max}$  in Step 4 is higher and the difference in the crack growth rates is much larger. This difference accumulates over 10,000 cycles, resulting at the end of the analysis in an overestimation of the delamination length by more than 3 mm.

The results of the analyses shown above demonstrate the high sensitivity of the fatigue analysis, whether CF20 or any Paris law-based fatigue model, to small differences in the characterization of the crack growth rates. A precise experimental characterization of the rates of propagation is essential to correctly predict delamination length as a function of the number of cycles.

## 8 | SUMMARY AND CONCLUDING REMARKS


The validation of the recently developed CF20 fatigue cohesive model was performed using a partially reinforced double cantilever beam (R-DCB) test reported in literature. This carefully controlled benchmark for mode I fatigue delamination propagation is similar to a DCB, but reinforcements bonded on the two arms induce variations in the local crack opening displacements that alter the rates of propagation of the delamination and induce several reversals of the curvatures of the delamination front as the delamination propagates. Most importantly, the benchmark includes the input data needed for analysis, such that a true model validation can be

conducted without calibrations based on the desired result. The parameters of the model were obtained from experimental crack growth rates of conventional DCB specimens. The comparison with the experimental results of three different specimens demonstrate the ability of the model to predict the crack growth rate and the delamination shape changes during propagation. Finally, a parametric study was performed to evaluate how the fatigue model responds to small perturbations of its parameters. The analysis results show that apparently minor differences in the characterization of the experimental crack growth rates can result in rather large differences in the predicted size of the delamination.

## ACKNOWLEDGMENT

The first author has received funding from the European Union's Horizon 2020 research and innovation program under the Marie Skłodowska-Curie grant agreement no. 707404.

## ORCID

Antonio Raimondo  <https://orcid.org/0000-0002-1122-9519>

Chiara Bisagni  <https://orcid.org/0000-0002-8713-9763>

## REFERENCES

1. Bisagni C, Vescovini R, Dávila CG. Development of a single-stringer compression specimen for the assessment of damage tolerance of postbuckled structures. *J Aircraft*. 2011;48(2): 495-502.
2. Pradhan SC, Tay TE. Three-dimensional finite element modeling of delamination growth in notched composite laminates under compression loading. *Eng Fract Mech*. 1998;60(2): 157-171.
3. Nixon-Pearson O, Hallett S, Withers P, Rouse J. Damage development in open-hole composite specimens in fatigue. Part 1: experimental investigation. *Compos Struct*. 2013;106: 882-889.
4. Mohlin T, Blom AF, Carlsson LA, Gustavsson AI. Delamination growth in a notched graphite/epoxy laminate under compression fatigue loading. In: Johnson WS, ed. *Delamination and Debonding of Materials, ASTM STP 876*. Philadelphia: American Society for Testing and Materials; 1985.
5. Sachse R, Pickett A, Essig W, Middendorf P. Experimental and numerical investigation of the influence of rivetless nut plate joints on fatigue crack growth in adhesively bonded composite joints. *Int J Fatigue*. 2017;105:262-275.
6. Dávila CG, Bisagni C. Fatigue life and damage tolerance of postbuckled composite stiffened structures with initial delamination. *Compos Struct*. 2017;161:73-84.
7. Dávila CG, Bisagni C. Fatigue life and damage tolerance of postbuckled composite stiffened structures with indentation damage. *J Compos Mater*. 2018;52(7):931-943.
8. Murri GB, Schaff JR, Dobyns AL. *Fatigue and Damage Tolerance Analysis of a Hybrid Composite Tapered Flexbeam*. Washington D.C: American Helicopter Society Forum; 2001.

9. Zhang B, Allegri G, Hallett SR. Embedding artificial neural networks into twin cohesive zone models for composites fatigue delamination prediction under various stress ratios and mode mixities. *Int J Solids Struct.* 2021;236-237:111311.
10. Liang Y-J, Dávila CG, Iarve EV. A reduced-input cohesive zone model with regularized extended finite element method for fatigue analysis of laminated composites in Abaqus. *Compos Struct.* 2021;275:114494.
11. Carreras L, Renart J, Turon A, et al. A benchmark test for validating 3D simulation methods for delamination growth under quasi-static and fatigue loading. *Compos Struct.* 2019;210:932-941.
12. Turon A, Costa J, Camanho PP, Dávila CG. Simulation of delamination in composites under high-cycle fatigue. *Compos Part A-Appl S.* 2007;38(11):2270-2282.
13. Harper PW, Hallett SR. A fatigue degradation law for cohesive interface elements—development and application to composite materials. *Int J Fatigue.* 2010;32(11):1774-1787.
14. Teimouri F, Heidari-Rarani M, Haji Aboutalebi F. Finite element modeling of mode I fatigue delamination growth in composites under large-scale fiber bridging. *Compos Struct.* 2021; 263:113716
15. Voormeeren LO, van der Meer FP, Maljaars J, Sluys LJ. A new method for fatigue life prediction based on the thick level set approach. *Eng Fract Mech.* 2017;182:449-466.
16. Bak BLV, Turon A, Lindgaard E, Lund E. A simulation method for high-cycle fatigue-driven delamination using a cohesive zone model. *Int J Numer Meth Eng.* 2016;106(3):163-191.
17. Carreras L, Bak BLV, Turon A, Renart J, Lindgaard E. Pointwise evaluation of the growth driving direction for arbitrarily shaped delamination fronts using cohesive elements. *Eur J Mech A-Solid.* 2018;72:464-482.
18. May M, Hallett SR. A combined model for initiation and propagation of damage under fatigue loading for cohesive interface elements. *Compos Part A-Appl S.* 2010;41(12):1787-1796.
19. Nojavan S, Schesser D, Yang QD. An in situ fatigue-CZM for unified crack initiation and propagation in composites under cyclic loading. *Compos Struct.* 2016;146:34-49.
20. Pan X, Jiang Y, Li M, Su Z. Theoretical and numerical investigation of mode-I delamination of composite double-cantilever beam with partially reinforced arms. *Fatigue Fract Eng Mater Struct.* 2021;44(12):3448-3462.
21. Dávila CG, Rose CA, Murri GB, Jackson WC, Johnston WM. Evaluation of fatigue damage accumulation functions for delamination initiation and propagation. In: *Technical Publication NASA/TP-2020-220584.* Hampton, VA; 2020.
22. Dávila CG. From S-N to the Paris law with a new mixed-mode cohesive fatigue model for delamination in composites. *Theor Appl Fract Mec.* 2020;106:102499
23. Allegri G. A unified formulation for fatigue crack onset and growth via cohesive zone modelling. *J Mech Phys Solids.* 2020; 138:103900
24. Dassault Systèmes. *Abaqus® 2017 Documentation.* Providence, RI, USA: Simulia Corp.; 2017.
25. Renart J, Budhe S, Carreras L, Mayugo J, Costa J. A new testing device to simultaneously measure the mode I fatigue delamination behavior of a batch of specimens. *Int J Fatigue.* 2018;116:275-283.
26. Carreras Blasco L. *Development of Efficient Testing Methods and Cohesive Zone Models for Analyzing Fatigue-Driven Delamination in 3D Laminated Composite Structures.* PhD Thesis, AMADE Research Group, U. of Girona, Spain; 2018.
27. Reeder JR, Demarco K, Whitley KS. The use of doubler reinforcement in delamination toughness testing. *Compos Part A-Appl S.* 2004;35(11):1337-1344.

**How to cite this article:** Raimondo A, Dávila CG, Bisagni C. Cohesive analysis of a 3D benchmark for delamination growth under quasi-static and fatigue loading conditions. *Fatigue Fract Eng Mater Struct.* 2022;45(7):1942-1952. doi:[10.1111/ffe.13712](https://doi.org/10.1111/ffe.13712)